Diurnal Patterns of Rainfall in Northwestern South America. Part II: Model Simulations

THOMAS T. WARNER

Program in Atmospheric and Oceanic Sciences, University of Colorado, and the Research Applications Program, National Center for Atmospheric Research, Boulder, Colorado*

BRIAN E. MAPES

NOAA–CIRES Climate Diagnostics Center, Boulder, Colorado

MEI XU

Program in Atmospheric and Oceanic Sciences, University of Colorado, and Research Applications Program, National Center for Atmospheric Research, Boulder, Colorado*

(Manuscript received 10 January 2002, in final form 29 August 2002)

ABSTRACT

This second paper of a three-part series documents the ability of the fifth-generation Pennsylvania State University–NCAR Mesoscale Model (MM5) to successfully replicate some known aspects of the rainfall of northwestern South America. The success of the control simulation justifies the use of the model in Part III for sensitivity experiments and more detailed diagnosis. The simulation is produced using multiply nested grids, with grid increments from 72 km down to 2 km. Three coarser-resolution grids are integrated for a period of 10 days, with the finest-resolution grid run for a 2-day subset of that period.

Several features of the rainfall field are examined as metrics of the model's performance. On the largest scales, the model reasonably simulates easterly waves in the western Atlantic and Caribbean, although it tends to develop them into tropical cyclones too readily. Over the Amazon River basin, diurnally initiated rainbands are observed to propagate westward, crossing the basin in 2–3 days. The simulation contains a similar phenomenon, whose propagation appears to involve both moisture advection and ducted gravity wave dynamics in the presence of an easterly jet near the 700-hPa level. On a finer scale, the model replicates the diurnal shift in precipitation across the west coast of Colombia, with afternoon and evening convection over land, and oceanic convection that begins immediately offshore after midnight and moves out to sea through the morning. On the finest scale, the simulation contains what appears to be a hydraulic jump, as the leading edge of the cool maritime air of the sea breeze surmounts the low coastal mountain range and flows eastward into the Atrato valley, to the foot of the Western Cordillera of the Andes. A similar feature has been previously documented to occur in a narrow valley in western Colombia, between north–south-oriented ridges of similar dimension and distance inland.

1. Introduction

Part I of this three-part series (Mapes et al. 2003b) describes the rainfall climatology of northwestern South America and the surrounding area. Several intriguing mesoscale characteristics of this climatology invite attempts at explanation, including large spatial rainfall gradients that are presumably related to the underlying geography, and a distinctive diurnal cycle. Observations are doubly inadequate to the task of diagnosing the mesoscale dynamics that shape these patterns, since data are especially sparse in an area where especially fine resolution and accuracy would be needed. Instead, our approach is to examine fine-grid model simulations with realistic terrain and other boundary conditions. The fine grid is nested within coarser grids that connect the fine-grid solutions with regional and global circulations, in a dynamically self-consistent way. In order for such an exercise to yield convincing explanations of natural phenomena, a thorough evaluation is needed of the ability of the modeling system to represent the prevailing atmospheric processes. If the model reasonably replicates known features and phenomena, this increases our confidence that its solutions are representative of features and processes that are not well observed. This Part II

* The National Center for Atmospheric Research is partially sponsored by the National Science Foundation.

Corresponding author address: Thomas T. Warner, NCAR/RAP, P.O. Box 3000, Boulder, CO 80307-3000.
E-mail: warner@ucar.edu

of the series describes our control simulation results and compares them with observed climatological features of the area. The veracity of the model will justify its use in the more detailed diagnosis and sensitivity experiments described in Part III (Mapes et al. 2003a).

In addition to the time-mean rain, we compared the model solution with four other major features of the observed rainfall climatology of northern South America. First and foremost is the rainfall near the Pacific coast of Colombia, the rainiest area in the Americas, and arguably in the world (Poveda and Mesa 2000; Snow 1976). The diurnal pattern in this area features afternoon and evening rainfall inland, and late night and morning rainfall offshore, over the Panama Bight (see map in Fig. 1 of Part I). Another distinctive characteristic of the climatological rainfall of this area is the strong gradient on the southern edge. For example, Buenaventura, Colombia, on the coast at 3°53′N receives 6.38 m annually, while coastal Manta, Ecuador, at 0°57′S is semiarid with 0.28 m annually. Also, the eastern edge of the nocturnal and morning rainfall coincides curiously well with the coastline (Figs. 6–8 of Part I).

A second finescale feature of climatology that will be contrasted with the model solutions is the phenomenon described by Lopez and Howell (1967), in which vigorous and localized late afternoon and evening convection develops in narrow valleys near the coast. The counterintuitive fact is that the convection is located in the valley rather than over elevated terrain. Their hypothesis was that the westerly moist ''recurved trades,'' and the superposed inland flow of the daytime seabreeze circulation, can penetrate deeply inland at low levels, unhampered by the easterly trades that are blocked by the Andes to the east. Where the air can pass across north–south-oriented mountain barriers, a katabatic wind develops on the eastern slopes, and an associated hydraulic jump initiates convection on the downwind side of the valley. Through analysis of rainfall, cloud, and vegetation data, Lopez and Howell (1967) documented the effects of the katabatic wind and hydraulic jump in the Cauca valley between the Western and Central Cordilleras of the Andes. Where low passes in the Western Cordillera allow passage of the westerly flow, the conditions are especially dry and cloud free on the eastern slopes, and local rainfall maxima prevail in the climatology on the floor and opposite side of the Cauca valley.

A third aspect of the observed rainfall to be employed for model verification in the existence of diurnal rainbands that propagate westward across the Amazon basin, as seen in Fig. 11 of Part I. These rainbands can maintain their integrity for 2–3 days as they propagate westward from their genesis in northeastern South America to near the eastern slopes of the Andes. Although their impact on the area west of the Andes is unclear, these bands do approach the eastern boundary of our finer grids. In any case, they provide a test of model dynamics on the model's coarsest grid, with implications for the accuracy of the nested-grid approach. A fourth model–data comparison, also on a coarse grid, is of easterly waves that were observed in the Northern Hemisphere trades.

In addition to these comparisons of climatological rainfall and rain-producing weather, the model solution has been compared with direct observations at selected surface and upper-air sites. The diurnal temperature cycle in the model is important to the fidelity of its diurnal cycle of circulation, convection, and rainfall.

Section 2 describes the modeling system, section 3 summarizes the experimental design of the control simulation presented here, and section 4 compares the control simulation with observations and climatological features. Section 5 provides a discussion and summary of the results.

2. Description of the modeling system

The model used in this study is the fifth-generation Pennsylvania State University–National Center for Atmospheric Research (Penn State–NCAR) nonhydrostatic Mesoscale Model (MM5). For details about this modeling system refer to Dudhia (1989, 1993), Grell et al. (1994), and Warner et al. (1992). The quadruply nested computational grids are depicted in Fig. 1. Grids 4 (the inner grid), 3, 2, and 1 (the outer grid) have mesh sizes of 209 × 321, 136 × 181, 91 × 124, and 61 × 121 points and grid increments of 2, 8, 24, and 72 km, respectively. The nested grids each have 32 vertical computational layers, and the outer three grids interact during the simulation. For computational reasons, grid 4 is run separately, after the outer three grids, with boundary values based on a linear spatial and temporal interpolation between 3-h simulated fields passed from grid 3. The model top is located at 50 hPa in MM5's reference atmosphere, which corresponds to about 110 hPa in this warmer tropical atmosphere.

The planetary boundary layer parameterization, based on Hong and Pan (1996), is the ''nonlocal'' technique that is employed in the Medium-Range Forecast (MRF) model of the National Centers for Environmental Prediction (NCEP). A simple explicit treatment of cloud microphysics is employed and is based on Dudhia (1989). Both ice and liquid phases are permitted for cloud and precipitation, but mixed phases are not permitted. The model uses a radiation scheme in which longwave and shortwave radiation interact with the clear atmosphere, cloud, precipitation, and the ground (Dudhia 1989), although terrain slope and aspect effects are neglected in ground radiation.

For the convective parameterization (CP), the Kain–Fritsch scheme (Kain and Fritsch 1990, 1992, 1993) was used on the outer three grids, with no parameterization employed on the inner grid. Other CPs were tested, as described in the next section and in Mapes et al. (2003, manuscript submitted to *J. Atmos. Sci.*, hereafter MWX).

The land surface model (LSM) used in the MM5 sys-

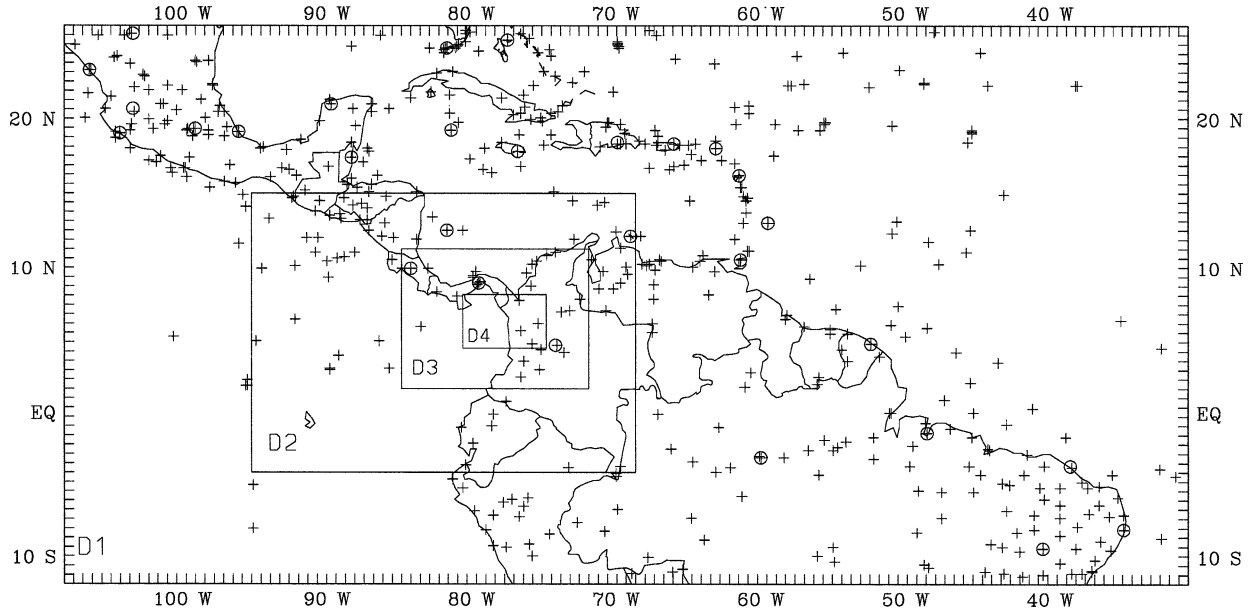

FIG. 1. Base map of model computational grids, labeled D1–D4. The plus signs indicate the locations of surface observations, and the circles define the locations of radiosonde observations.

tem is based on the diurnally dependent Penman potential evaporation approach of Mahrt and Ek (1984), the multi-layer soil model of Mahrt and Pan (1984), and the primitive canopy model of Pan and Mahrt (1987). It has been extended by Chen et al. (1996) to include the canopy-resistance approach of Jacquemin and Noilhan (1990) and the surface runoff scheme of Schaake et al. (1996). It has one canopy layer and the following prognostic variables: volumetric soil moisture and temperature in four soil layers, water stored on the canopy, and snow stored on the ground. The depths of the soil layers are 0.1, 0.3, 0.6, and 1.0 m, from the top layer to the bottom layer, respectively. The root zone is in the upper 1 m of soil, and the lower 1 m of soil acts like a reservoir with gravity drainage at the bottom. A summary of this LSM and its use in MM5 can be found in Chen and Dudhia (2001a,b).

The surface landscape characteristics are defined based on four datasets. The United States Geological Survey (USGS) Earth Resources Observing System (EROS) 1-km dataset (Loveland et al. 1995) is used to define the vegetation type, and the State Soil Geographic (STATSGO) 1° database is used for soil type (Miller and White 1998). Green vegetation fraction is defined based on a 15-km dataset derived from the Advanced Very High Resolution Radiometer (AVHRR). Terrain elevation is specified based on a 30 arc-second dataset. Figure 1 of Part I shows the terrain elevation for grids 1, 3, and 4, and the sea surface temperatures for grids 1 and 3. The initial values of the time-varying soil moisture and temperature profiles are based on the NCEP–NCAR 2.5° resolution reanalysis.

The sea surface temperatures (SSTs; Fig. 1 of Part I) were defined using a combination of satellite infrared radiances and the NCEP–NCAR 2.5° analysis. The satellite-based estimates, using *Geostationary Operational Environmental Satellite-11* (*GOES-11*) μ and *-12* μ channels, were computed using a split-window, multichannel SST equation, with coefficients derived at the Climate Diagnostics Center of the National Oceanic and Atmospheric Administration (G. Wick 1999, personal communication). The coefficients were empirically derived using cloud-free satellite radiances matched to buoy SST measurements obtained in 1997 and 1998. The algorithm was derived for use during both the day and night. The two analyses were combined by taking, for each model grid box, the maximum SST value from the two analyses. The rationale is that the infrared SST may be too low because of cloud contamination, in which case the presumably higher NCEP SST would be more representative. In fact, the two analyses did not differ markedly.

The model initial conditions are defined by analyzing radiosonde and surface data (see Fig. 1) to the model grids using a successive-correction objective analysis procedure (Benjamin and Seaman 1985), where the first guess field is the European Centre for Medium-Range Weather Forecasts (ECMWF) 2.5° analysis. Lateral boundary conditions for the outer grid (grid 1) are defined using linear temporal interpolation between 12-hourly ECMWF global analyses. Grids 1–3 were integrated for 10 days (see next section), while grid 4 was integrated for only 2 days during the second half of the period. Grid 4 was initialized based only on the grid-3 solution because of the paucity of data over this small area.

3. Experimental design and preliminary test simulations

Part I described the choice of a 10-day period for this study (1200 UTC 28 August–1200 UTC 7 September 1998), and showed it to be fairly representative of seasonal climatology, but with more active weather. Model grids 1, 2, and 3 were integrated continuously for this entire period. Grid 4 was integrated for a 2-day subset of this period, the second day of which had the strongest signal in the diurnal oscillation of the rainfall across the Pacific coastline at 5°–7°N. This period from 1200 UTC 1 September through 1200 UTC 3 September 1998 corresponds to days 5 and 6 of the 10-day integration on the outer grids. Most grid-4 diagnostics were performed using model output from the second day of the 2-day period.

In addition to establishing the study period and nested grid layout, other preliminary steps in this investigation involved defining a model configuration (mainly, the suite of physical parameterizations) to produce simulations of reasonable accuracy, as judged against available data and subjectively interpreted infrared satellite imagery. In the following subsections are briefly described some aspects of the model that were tested in the process of arriving at a final configuration. Not described are routine adjustments of the computational domain size and position, and shorter test simulations for other time periods.

a. Testing of different convective parameterizations

Initially, we followed the guidance in standard MM5 documentation, where recommendations for the choices among several available convection schemes are based on the range of horizontal resolution for which each scheme has been designed and most widely tested. Consequently, different parameterizations are recommended on adjacent grids of the nest, which have different grid increments. We found that the resulting horizontal contrasts in convective physics tended to produce unrealistic model solutions near the interfaces of the grids (as in Warner and Hsu 2000).

For example, the first test configuration of the model employed the Anthes–Kuo (Anthes 1977) convective parameterization on grid 1, with the Kain–Fritsch scheme (Kain and Fritsch 1990, 1992, 1993) on grid 2. Heavy rainfall was simulated on grid 2 along the boundary with grid 1, especially in the corners. Another ''mixed parameterization'' configuration used the Grell (1993) parameterization on grid 2, with the same Anthes–Kuo scheme on grid 1. The grid 2 rainfall from the Grell scheme seemed unrealistically concentrated over small areas, so that even the 10-day mean rainfall field was excessively spotty. The use of the Kain–Fritsch parameterization on both grids 1 and 2 produced the best overall solution when compared with GOES Precipitation Index (GPI; see Part I) rainfall and satellite cloud data. Later and more quantitative tests of these convection parameterizations reported in MWX also favored the Kain–Fritsch scheme with enhanced entrainment.

b. Parameterized versus explicit convection on the 8-km grid

For the 8-km grid increment on grid 3, the scale-separation assumptions of convective parameterizations are clearly questionable (Molinari and Dudek 1992). On the other hand, the resolution is too poor to explicitly resolve convection well. Wang and Seaman (1997) have shown that the use of the Kain–Fritsch parameterization and a grid increment of 12 km produces reasonable precipitation simulations for midlatitudes. Thus we were encouraged to try the Kain–Fritsch parameterization with the 8-km grid increment. In fact, the parameterized rainfall on grid 3 compared better (qualitatively) with satellite cloud imagery than did the rainfall from the explicitly represented but poorly resolved convection. In particular, the explicit convection at this resolution was too spotty, and it initiated too late in the day. In summary, the best result was obtained when all three outer grids (with 72-, 24-, and 8-km increments) employed the Kain–Fritsch scheme.

c. Sensitivity of the Kain–Fritsch parameterization to internal parameters

This parameterization has been used in other tropical MM5 simulations (e.g., Vizy and Cook 2002), but has undergone more exhaustive testing for midlatitude convection. The standard Kain–Fritsch scheme, in this application, produced rain too easily over wide areas, producing a smooth and muddy pattern of rainfall. Also, there was explosive convective spinup on the first day of the simulation, and rapid development of upper-level divergence that was much too strong, in the sense that it was inconsistent with the mean regional-average divergence implied by the lateral boundary conditions from the ECMWF global analysis (MWX). These symptoms point to the convection scheme being insufficiently restrained by the buoyancy-reducing effects of mixing. As a remedy, the specified radius of the updraft core in the parameterization was reduced from 1500 m, normally used for midlatitude continental convection, to 750 m, which increases the mixing between the updraft and ambient air. This largely eliminated the noted problems, although the altitude of upper-level divergence became too low (MWX).

d. The 1-day spinup period for the grid-4 simulation

The grid-4 solution is presented here for one diurnal period, from 1200 UTC 2 September to 1200 UTC 3 September 1998 (beginning and ending at roughly 0700 LT). This is the second day of the 2-day simulation

on grid 4, and the sixth day of the grids 1–3 simulation. Thus, grid 4 has 1 day after the initialization from the grid-3 solution to ''spin up'' before the results are used for diagnostics. One aspect of the spinup is that the grid-4 fields are initialized from a smoother grid-3 solution, and thus better-resolved orographically and coastally forced structures need time to develop. Another spinup consideration is that grid 3 employed the Kain–Fritsch parameterization while grid 4 had explicitly resolved convection only. Thus, the vertical structure of temperature and humidity on grid 4 needed time to adjust to the different convective physics. In order to ensure that the 1-day spinup period was sufficient, grid 4 was initialized 1 day earlier at 1200 UTC 31 August 1998 and run for 3 days. The results from day 3 of this experiment were very similar to those from day 2 of the other, indicating that 1 day is long enough for spinup.

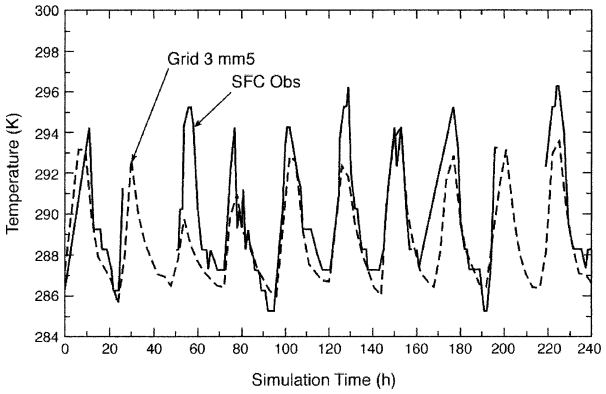

FIG. 2. Model-simulated and observed screen-level temperature for the observation location nearest the eastern boundary of grid 4 (see Fig. 1), for the 10-day simulation period. The dashed line indicates the simulated temperature from domain 3, and the solid line shows the observations. Note that there are two periods of approximately 1 day each for which data were not available.

4. The numerical simulation and comparison with observations

The density of surface and radiosonde observations (Fig. 1) is sufficient for construction of an analysis of large-scale conditions, but it is not possible to obtain a good analysis of mesoscale features. Comparisons of model-simulated and observed values at a few individual points indicate reasonable agreement, although this is by no means a comprehensive test of the model. Also, we compare simulated rainfall with GPI infrared satellite rain estimates. Only qualitative rainfall comparisons can be made, since the GPI is only a climatologically validated product, and is inaccurate at subdiurnal timescales. Specifically, the GPI-based estimates lag actual rainfall by about 3 h, at least in Brazil (Negri et al. 2002). Moreover, it may excessively favor large long-lasting, cold-cloud shields, relative to their real contributions to rainfall. Lower-topped orographic cloud systems can produce copious rainfall over steep terrain. Still, comparison of GPI and other rainfall estimates indicates that it is a reasonable representation of true rainfall (see Part I for more discussion).

a. Comparisons with in situ data and wind analyses

The locations of surface and radiosonde observations within the area of the model simulations are shown in Fig. 1. Most of the surface stations provided some data during the 10-day period; however, the temporal resolution was sporadic, with the frequency sometimes being one observation per day. Because the processes that are the focus of this study seem to be diurnally periodic, a relevant measure of the veracity of the simulation of the heating cycle is the diurnal variation in temperature. The station on grid 4 nearest to the eastern boundary (Fig. 1) provided data with good temporal resolution, and its temperature data are compared with the model simulation in Fig. 2. The 1–2-K offset between the model and station data is quite small, in light of the uncertain representativeness of a point site in mountainous terrain. On most days, the model reasonably replicated the 8°–10°C amplitude of the diurnal temperature oscillation, with only a slight tendency to underestimate it on some days. With earlier model configurations, the diurnal temperature range was more drastically underestimated, after the initial convective spinup created a long-lasting overcast of cloud, so this test is not trivial.

Radiosonde soundings from Bogota, Colombia; Panama City, Panama; and San Jose, Costa Rica were also compared with the model solution for the irregular times that the data were available during the 10-day period (not shown). Simulated wind profiles compared reasonably well with these point observations. More illuminating wind comparisons are discussed below. In thermodynamic profiles through the midtroposphere, the simulated and observed temperature and dewpoint had differences that were fairly small in light of the sampling uncertainties. The greatest discrepancies were in dewpoint above 300 hPa, but radiosonde humidity sensors are unreliable at those levels. The model seemed to burn off the temperature inversion too early in the day at Bogota, perhaps because the 8-km grid increment cannot satisfactorily resolve topographic irregularities that can affect inversion depths. In short, radiosonde comparisons were satisfactory but not very discriminating tests of the model's performance.

Maps of low-level winds from MM5 and the ECMWF global reanalysis are shown in Fig. 3, for day 6 of the simulation (0000 UTC 3 September 1998). Model winds near the boundaries are nudged toward this analysis, so similarity is inevitable, but in the domain interior the winds can differ substantially, as determined by the model's physics and dynamics. The degree of potential disagreement is il-

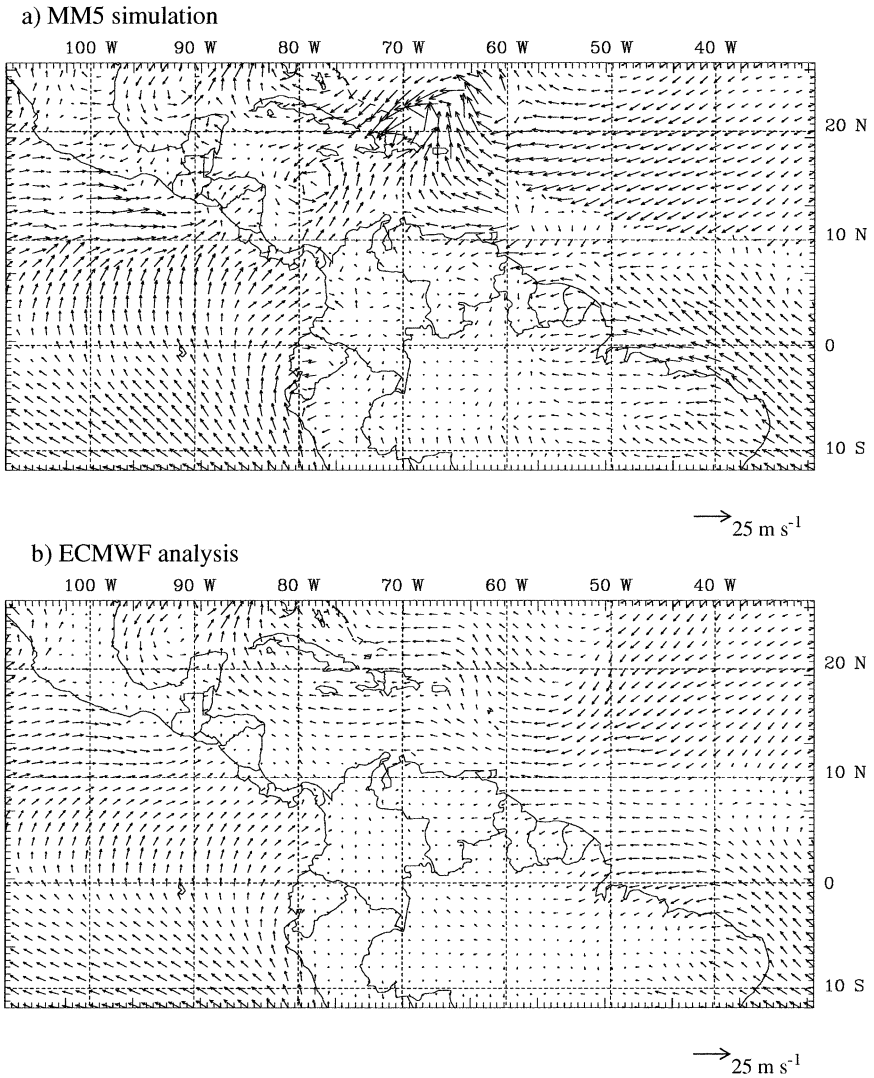

FIG. 3. Low-level (40 m AGL) wind flow for 0000 UTC 3 Sep 1998, during day 6 of the simulation. (a) MM5 simulation on domain 1. (b) ECMWF analysis.

lustrated by the model's two simulated cyclones in the Caribbean Sea, with winds up to 25 m s^{-1}, which were not observed to occur. The tendency of MM5 to spin up coarsely resolved tropical cyclones too readily has been noticed by other users as well (e.g., Swanson 1998). In our main area of focus, along the Pacific coast of South America, the simulated and analyzed low-level flow agree much better, and both are quite similar to the August climatological-mean surface winds of Sadler (1986), shown in Fig. 4 of Part I. Southeasterly winds are parallel to the coast in northern Peru. From Chiclayo, Peru (about 5°S), northward, the winds begin to develop a slight westerly inland component that becomes more pronounced in the Panama Bight, then slows (converges) near the Colombian coast.

b. Comparisons of rainfall patterns

For rainfall verification, we begin with the simulated 10-day mean for the study period on our largest domain, grid 1 (Fig. 4). This may be compared directly to the GPI observational estimate (Fig. 10a of Part I). At the grossest scales, the patterns of rainfall are similar, with maximum rainfall north of the equator in the eastern Pacific and little or none in the Southern Hemisphere. Excessive rainfall was simulated in the Atlantic basin, especially in the northern part of the domain. Here the excessively strong tropical cyclones reached their maximum development, before being relaxed away by the nudging of fields toward the ECMWF analysis in the rows of grid points adjacent to the boundary. Excessive rainfall was also simulated in a patch along 6°–10°N at

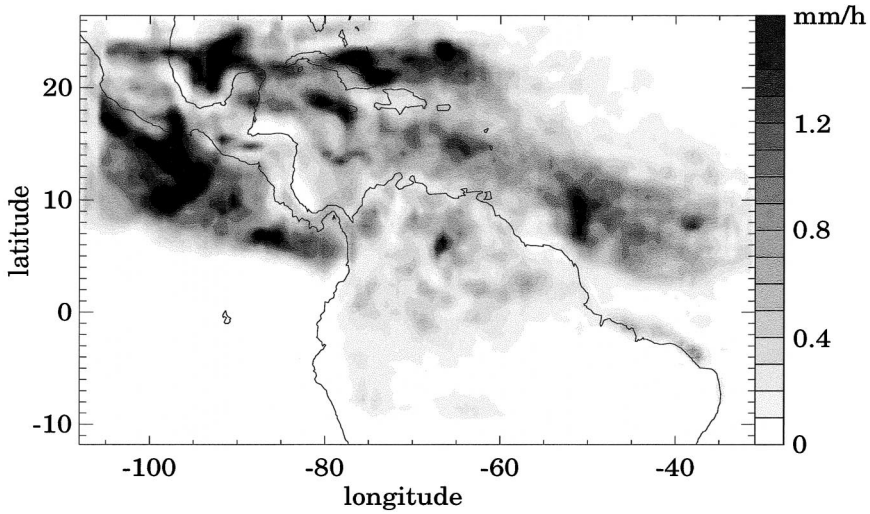

FIG. 4. Simulated 10-day-average rain rate on domain 1. Compare to Fig. 10a of Part I.

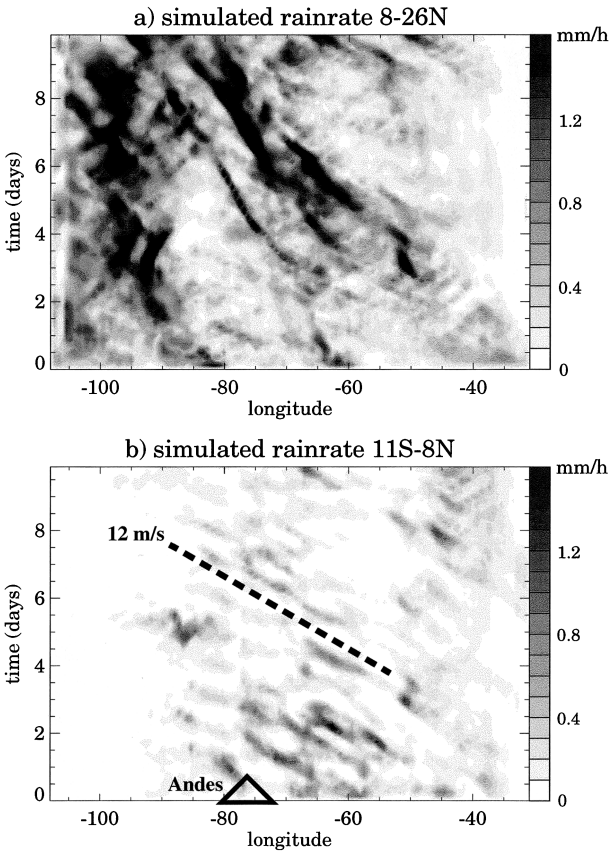

FIG. 5. Time–longitude plots of domain-1 rainfall for the 10-day period of the simulations. (a) Northern half of the domain, 8°–26°N. (b) Southern half, 11°S–8°N, with symbolic indication of the Andes location and 12 m s^{-1} propagation speed. Compare to Fig. 11 of Part I, or more exactly to Fig. 2 of MWX.

50°W, and at a point near the crest of the Guiana Highlands at 6°N, 65°W. In the region of the finer grids 2 and 3 (in which the finer-grid solutions overwrite the fields computed directly on grid 1), the simulated rainfall is recognizably similar to observations (analyzed further below), although with less rainfall simulated in the southern concavity of the Panama Bight.

The temporal pattern of simulated rainfall is shown in Fig. 5, for the northern and southern halves of our largest domain. These may be compared with the GPI observations of Fig. 11 of Part I. In the northern half (Fig. 5a), enhanced rainfall occurs in three disturbances that move westward with time, near 80°, 60°, and 35°W at the initial time. These three observed rainfall features are replicated in the model, even though the model initial and boundary fields contain only wind and thermodynamic state variables. The tendency for the model to overdevelop these easterly disturbances is again seen in Fig. 5a, in the form of excessively intense precipitation features. In the southern half of the large domain (Fig. 5b), a strong diurnal cycle is seen over the South American continent. Westward propagation is prominent, with a typical speed of about 12 m s^{-1} as indicated by the sloping line. Similar westward propagating precipitation features are seen in observations, and are known as Amazonian squall lines (Greco et al. 1990; Garstang et al. 1994; Cohen et al. 1995). Propagation mechanisms of Amazon squall lines in the model are examined in the appendix of this paper.

An especially important test of the model for present purposes is its mean diurnal cycle of rainfall in northwestern South America. Figure 6 displays the 10-day average grid-2 simulated rainfall at 3-h intervals, to be compared qualitatively with Fig. 8 of Part I. Starting near local midnight, strong rainfall in the Magdalena Valley (8°N, 75°W) diminishes through the night, as convection develops just offshore of both the Pacific

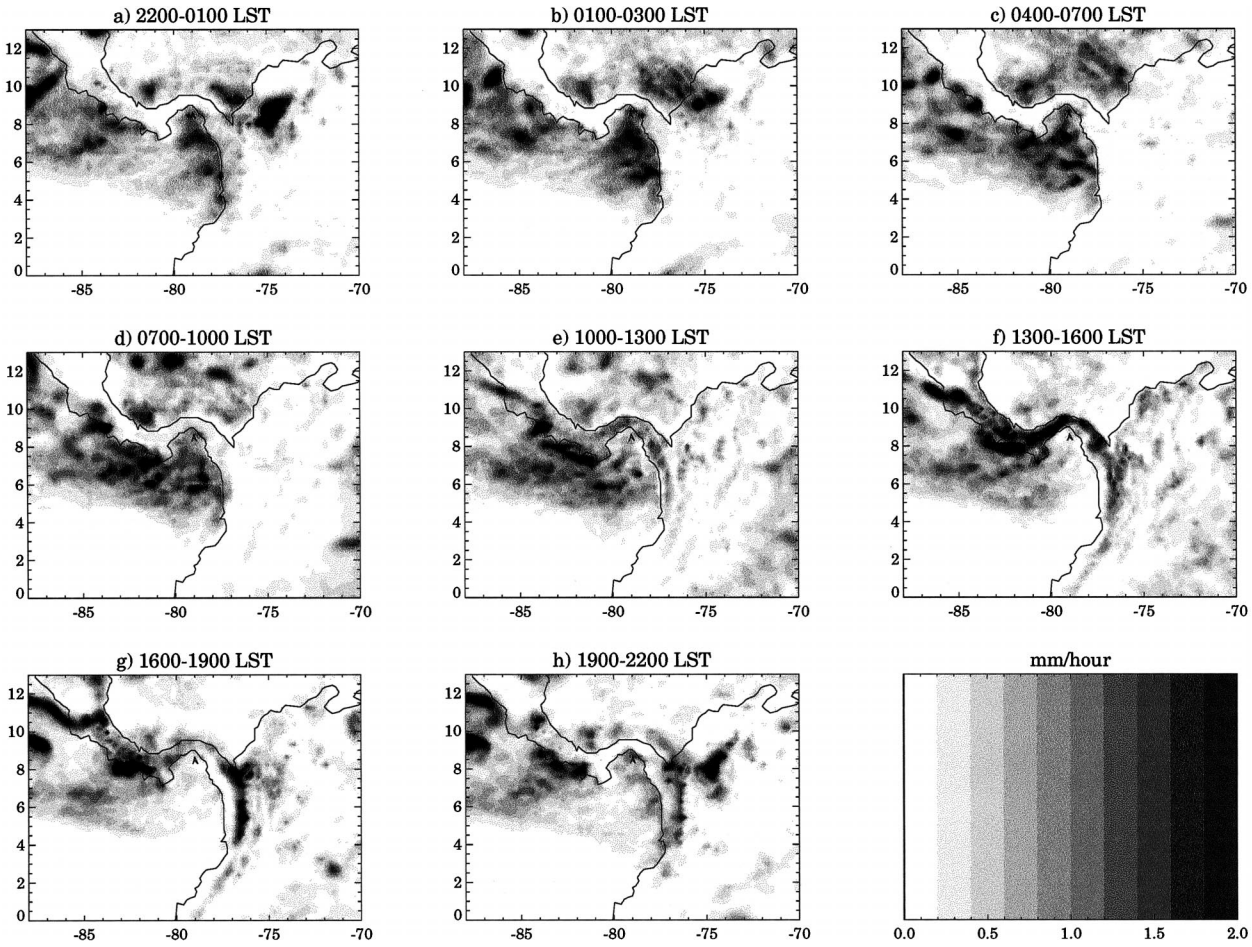

FIG. 6. Ten-day mean diurnal cycle of domain-2 rain rate for the local times shown. Compare qualitatively to Fig. 8 of Part I.

and Caribbean coasts of Colombia (Figs. 6a,b). During the morning hours, this maritime rainfall propagates in a locally offshore direction, with a larger-scale tendency for westward propagation in both ocean basins (Figs. 6c,d). During the afternoon, convection develops over land, especially over mountains not far inland (Figs. 6e–g). In late evening, this mountain rainfall decreases, and rainfall increases over the large Magdalena Valley and Lake Maracaibo (Fig. 6h). All of these features are in qualitative agreement with the observations. Quantitative comparisons are difficult on small scales, but it is worth noting that the domain-average rainfall rate on grid 2 for the 10-day period is 10.4 mm day^{-1}, compared to 9.2 mm day^{-1} for GPI for the same domain and period.

Most important for our purposes, the model captures the observed diurnal land–sea oscillation in rainfall along the Pacific coast of Colombia, with the intense maritime rainfall between roughly midnight and noon, and the clearing off the coast as the convection develops over the mountains during the day. The simulation also represents well the observed very sharp eastern boundary of the maritime rainfall, closely corresponding to the position of the coastline. Daily average rain rate, corresponding to the average over all the panels in Fig. 6, may be seen in Fig. 3 of Part III.

To better visualize the similarity in the simulated and GPI-estimated east–west diurnal shifts in the rainfall over the grid 2 area, Fig. 7 shows time–longitude sections of rain rate for the 3°–7°N band, directly comparable to Fig. 12 of Part I. The mean diurnal patterns of simulated and climatological GPI-estimated rainfall (panel a in each figure) are very similar, including the evening maximum in the coastal lowlands and the aftermidnight development and ~15 m s^{-1} westward spread from the coastline of the maritime rainfall. Major differences are 1) the rainfall maximum to the east of the Andes (near 70°W) is 3–4 h earlier in the simulation, 2) the nocturnal rainfall over the upper Magdalena Valley (74°–75°W) is lighter and dissipates earlier in the simulation, and 3) the simulated rainfall on the west slopes of the Andes near 2000 LT (just to the east of the coastline) is much heavier, more focused, and longer lasting than that based on the GPI. Some of these differences could be attributable to shortcomings of the GPI rainfall estimate.

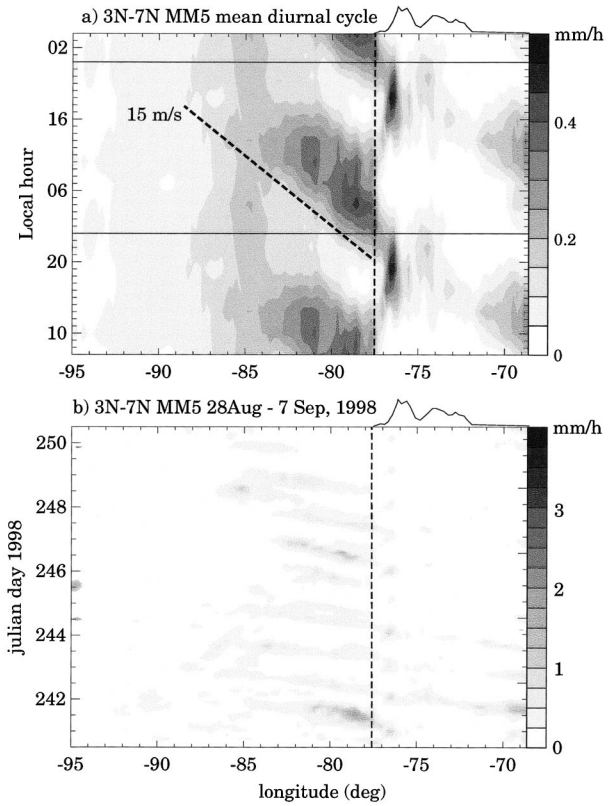

FIG. 7. Time–longitude plot of domain-2 rain rate for the 3°–7°N band. (a) Mean diurnal cycle, repeated twice for visual clarity. (b) The 10 individual days of simulated rainfall. Vertical dashed lines represents the location of the coast, and mean terrain elevation is indicated schematically atop the plot frames. Compare to Fig. 12 of Part I.

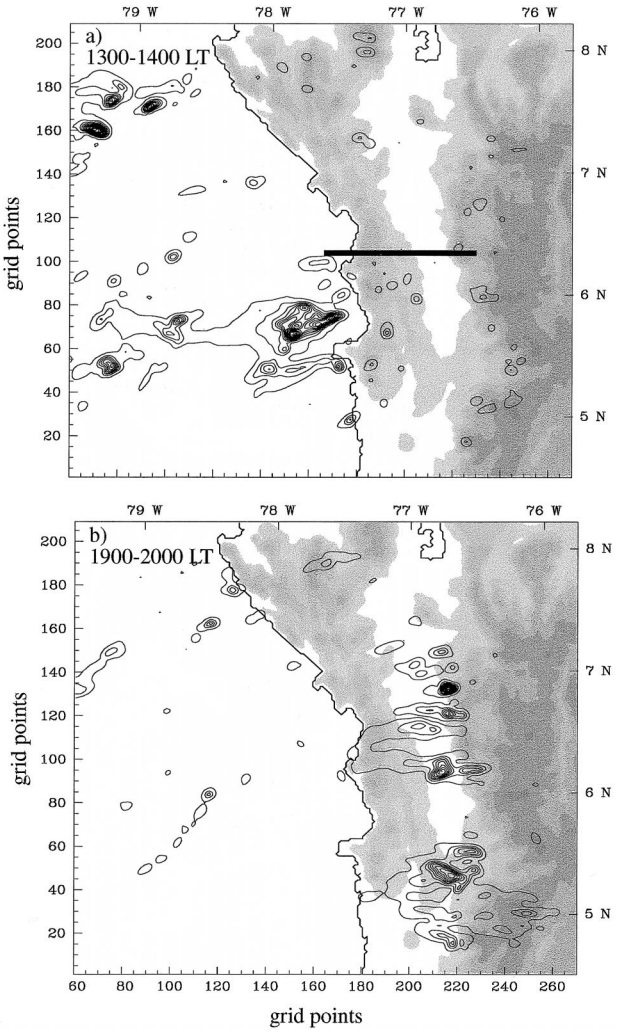

FIG. 8. Model-simulated hourly rainfall (contours, 5 mm h^{-1} interval) for the two times indicated, based on the grid-4 simulation for a subarea of that grid near the coast. The terrain is shaded, with darker grays indicating higher elevations. The heavy horizontal line segment indicates the location of the cross sections in Fig. 9.

Another substantial difference between the model and observations is seen in comparing Fig. 7b with Fig. 12b of Part I. Even though the mean GPI and model rainfall patterns are very comparable, the simulated rainfall pattern is more diurnally repetitive and considerably weaker than in the actual atmosphere. Note that Fig. 12a of Part I, which agrees fairly well quantitatively with Fig. 7a, is a 2-yr August–September mean. The particular 10 days of our simulation, in panel b of the two figures, had about twice as much GPI-estimated rainfall as did the simulation in the indicated domain. The simulation also has much less rain far offshore (e.g., 89°W) in this latitude band.

c. Sea-breeze processes in grid 4

These nested grid simulations culminate in the grid-4 simulation over the coastal zone of western Colombia, with a 2-km grid increment and no moist convection parameterization. Here the coastline and the nearby complex orography (Fig. 8; see also Fig. 1c of Part I for geographical names and larger-scale maps) induce low-level circulations with important impacts on the temporal and spatial distributions of mesoscale features in the rainfall. In the model simulations described here, we see processes that are quite similar to those documented by Lopez and Howell (1967), with the sea breeze spilling over near-coastal mountains into a valley ~100 km inland. In this case, these processes occur in the Atrato Valley between the Serrania de Baudo (coastal range in Fig. 8) and the Western Cordillera of the Andes, whereas Lopez and Howell discussed the Cauca valley to the east of the Western Cordillera, near 4°N where it is closest to the coast. The geometry of coasts and mountains is roughly similar in both settings. The grid-4 simulation will be used to illustrate these processes for the period 1200 UTC 2 September–1200 UTC 3 September 1998.

During the morning, the sea-breeze circulation and the upslope mountain-valley breeze augment the large-

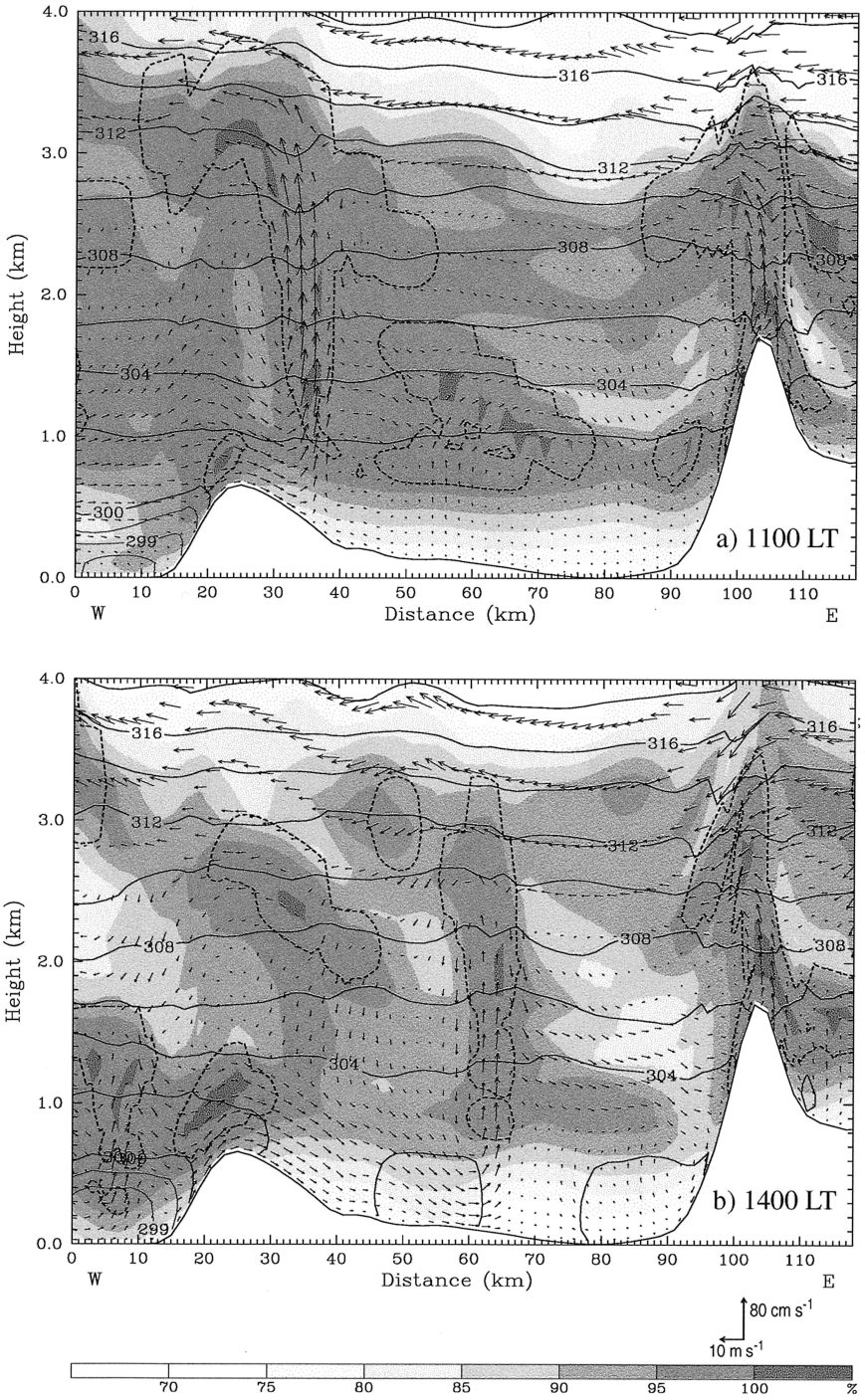

FIG. 9. Cross sections at the indicated times from day 2 of the domain-4 simulation, along the heavy line in Fig. 8. Relative humidity is shaded, with cloud boundary indicated by dashed curves. Arrows indicate wind components in the plane of the section (zonal and vertical). Potential temperature is contoured, at an irregular interval: 2° above 300°C and 0.5° below 300°C.

scale, low-level, generally westerly flow on the west face of the Serrania de Baudo. By late morning or early afternoon, depending on the proximity of the terrain maximum to the coastline, this westerly boundary layer flow surmounts the ridge. This situation is shown in Fig. 9a for 1100 LT. Depicted are the relative humidity, potential temperature, cloud, and wind vectors along a cross section defined by the line in Fig. 8. Rising motion

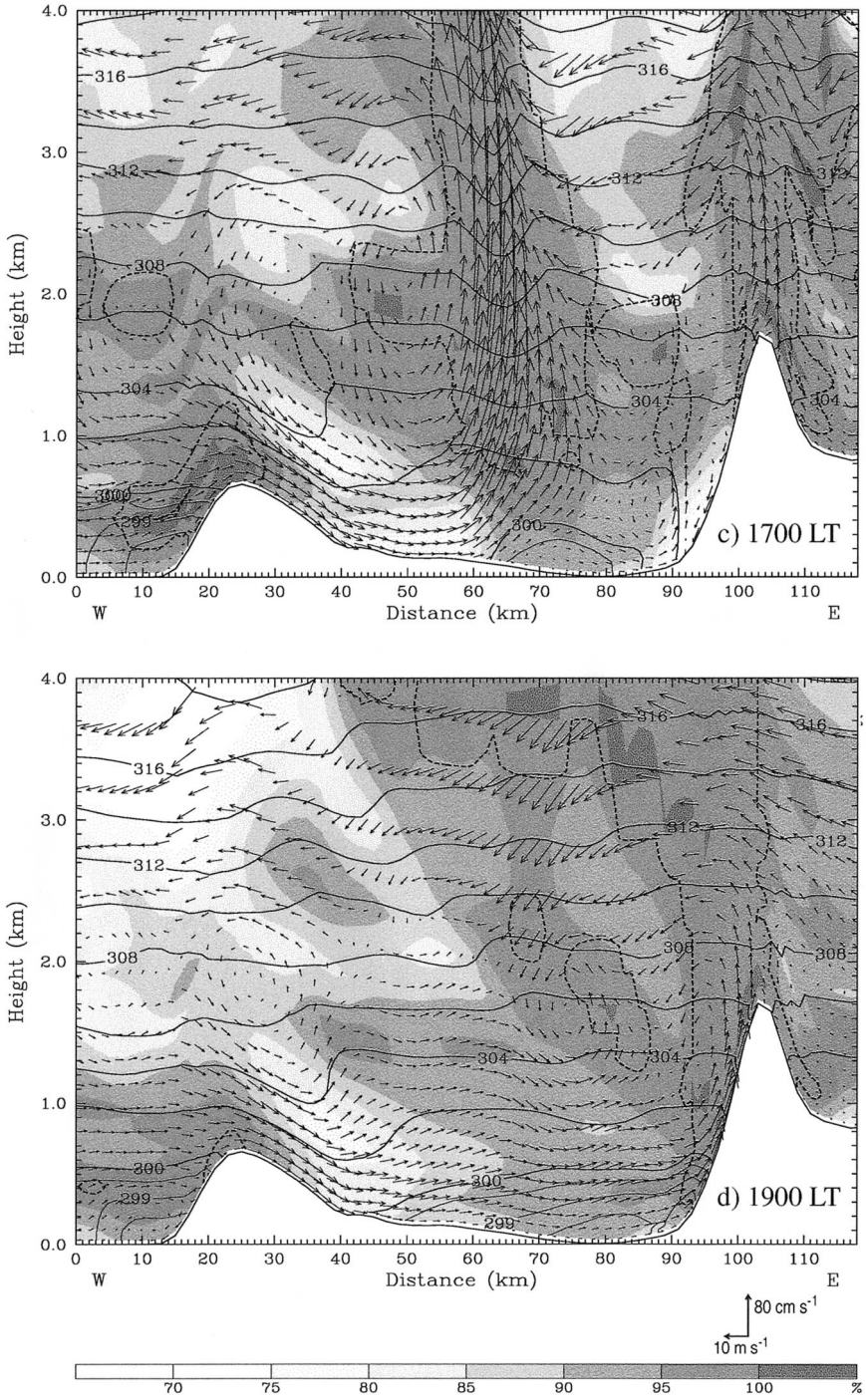

FIG. 9. (*Continued*)

and convection develop on the east side, where the sea breeze converges with weak easterly upslope flow that has developed on the east side, presumably as a reult of heating of the mountain slope but possibly augmented by gravity wave dynamics [cf. Figs. 16 and 17 of Tripoli and Cotton (1989), Fig. 7 of Satomura (2000)]. Convection is also seen over the Western Andes Cordillera from the mountain–valley breeze, reaching altitudes of 3–4 km. Shallow cloud exists over the valley. By 1400 LT, the convergence line and associated convection have moved about 30 km eastward into the valley (Fig. 12b). During the following 3 h, the convective cell slows its eastward movement and intensifies (Fig. 12c). For most of the day, the upward motion associated with this fea-

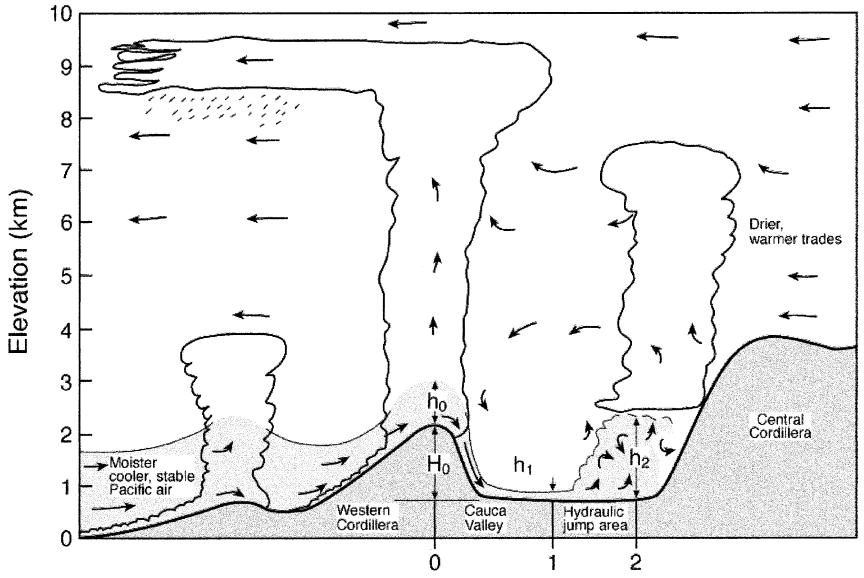

FIG. 10. Reproduction of the Lopez and Howell (1967) schematic of the observed convection in the Cauca Valley and the hydraulic jump that results from cool maritime air flowing over the Western Cordillera of the Andes, near 4°N. Horizontal scale is approximately 100–150 km.

ture has exceeded even that over the Western Andes Cordillera. During the early evening, enhanced westerlies still prevail in the valley (Fig. 12d), but dissipate to near calm before midnight.

The simulated diurnal pattern of the winds and convection in this cross section is generally typical of that prevailing along other cross sections for which there is significant coastal orography. In contrast, to the south of the Serrania where the land is flat between the coast and the Western Cordillera, the sea breeze flows gently and unperturbed until it encounters the Cordillera and initiates convection in the late afternoon. But, even where the Serrania achieves significant elevations between 5° and 7°N, there is much meridional variation in the details of the simulated processes on any particular day, especially in terms of rainfall accumulation. To illustrate, Fig. 8 shows hourly rainfall from grid 4 for early afternoon (1300–1400 LT) and early evening (1900–2000 LT). Consistent with the cross sections shown, the early afternoon rainfall over land is light, and occurs on the Atrato Valley side of the slopes of the Serrania and the Western Cordillera. By evening, heavy convective rainfall prevails in localized areas of the valley, with a preference for the eastern side. The 10-day-mean diurnal rainfall from grid 3 for this area reveals a similar pattern, but with the parameterized convection tending to simulate more rain earlier in the day (1000–1300 LT), over the Serrania (cf. Figs. 6e and 8a). Observations (Fig. 8 of Part I) have significant rain just beginning to appear in this area at 1400 LT. It is worth briefly noting that satellite imagery shows cold cloud tops developing over the Atrato valley in the late afternoon and evening of the day described, with the hint of some activity in the Cauca valley. There are no gauge data available for the Atrato valley, and too few elsewhere to characterize the real rainfall, but during the last week of the grids 1–3 simulation, total accumulations of about 2.5 cm were observed in some locations of the Cauca Valley.

Regarding the question about whether the convection-initiating convergence line during the daylight hours is associated with a sea-breeze front or katabatic flow (or a combination), it is perhaps revealing that the westerly boundary layer flow only develops to considerable strength after it crests the ridge of the Serrania (see Fig. 4 of Part III). It is sufficient for the purposes of this paper to point out that these results are consistent with the observations of Lopez and Howell (1967), except that we simulate the convective processes on this day to be one valley to the west of those described in Lopez and Howell. Figures 9c,d and the Lopez and Howell schematic of the late afternoon flow reproduced in Fig. 10 are strikingly similar except for the names of the valleys. On this day, kinematic trajectories based on the simulated three-dimensional wind field show that maritime air reaches the Western Cordillera in some latitudes, but does not cross it. During other periods with different prevailing large-scale static stability and/or greater strength to the low-level westerly flow, it is reasonable that the flow could crest the Western Cordillera, and surge into the Cauca valley to the east to produce the convection that Lopez and Howell documented there.

During the late evening and night hours, the simulated valley convection diminishes in intensity, but a residual area of lower rainfall intensity curiously broadens westward toward the coast, as though in response to developing forces that will cause the near-coast maritime rain-

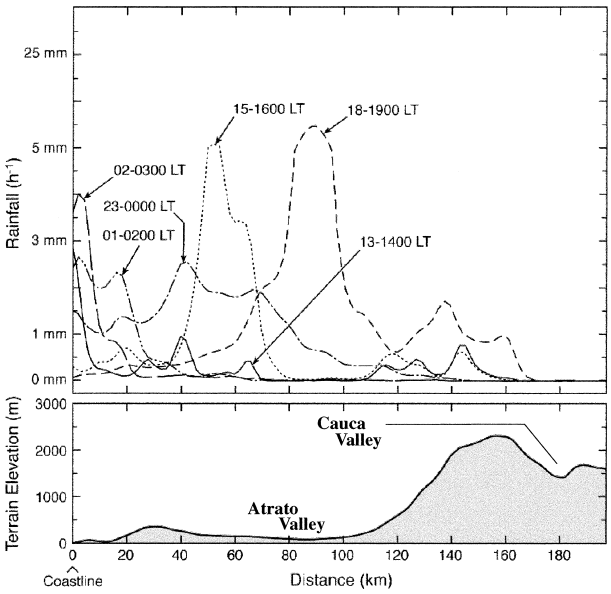

FIG. 11. Model-simulated hourly rainfall on grid 4 for the various periods shown during the diurnal cycle, averaged over approximately a 1° latitude belt that is centered on the cross sections of Fig. 9 (heavy line in Fig. 8). The terrain elevation is shown at the bottom of the figure.

fall to blossom a few hours later (the subject of Mapes et al. 2003a, hereafter Part III). To illustrate, Fig. 11 shows the hourly rainfall for various times during the diurnal cycle, averaged over approximately a 1° latitude belt of the Serrania, centered on the transact over which Fig. 9 applies.

5. Discussion and summary

The purpose of this paper is to demonstrate the veracity of the model, to justify its suitability for physical process studies in Part III. Thermodynamics, wind, and rainfall features at several scales have been used as criteria by which we judge the model's adequacy for the forensic analysis to follow.

The diurnal temperature cycle over land is reasonably reproduced (Fig. 2). The wind field in the Pacific is close to the observed (Fig. 3), although Atlantic disturbances developed too strongly into coarsely resolved tropical cyclones (Figs. 3, 5a). These tropical cyclones produce significant errors in the time-mean large-domain rainfall (Fig. 4), but not enough to completely distort or invalidate the solutions on the finer grids. The coarse (72 km) mesh with parameterized convection successfully simulates propagating Amazon squall lines, whose propagation mechanisms are explored in the appendix. Most importantly for Part III, the mean diurnal rainfall cycle over western Colombia and adjacent waters is reasonably well represented (Figs. 6, 7a). Unfortunately, the individual-day weather over western Colombia is too diurnally repetitive and weak (Fig. 7b), not reproducing the dynamic range of observations, with organized heavy precipitation events seen on 3 out of 10 days (Fig. 12b of Part I). The same shortcoming characterizes the runs in which no convection scheme was used on the 8-km mesh of grid 3 (not shown).

Thus, without overstating the success of the triply nested coarser-grid simulation, we conclude that it does seem to provide sufficiently accurate initial and lateral boundary fields that our central three-dimensional convection-resolving simulation, on the 2-km mesh of grid 4, appears realistic. A particular aspect of the rainfall climatology of coastal Colombia is the diurnal shift in precipitation across the coastline, such that afternoon and evening rain prevail over land, with heavy late night and morning rain beginning at the coastline and moving offshore. The ability of the model to reproduce this phenomenon was demonstrated in this paper and is further examined in Part III. Also simulated well was the existence of afternoon and evening rainfall within the north–south-oriented narrow valleys, rather than over elevated terrain.

The diurnal cycle results from interactions of the land surface forcing with the large-scale flow. Therefore, it should not be surprising that a model should be able to simulate them, to the extent that it has reasonably accurate representations of 1) the large-scale flow, 2) the surface budgets of heat, moisture, and momentum, 3) the boundary layer dynamics that couple the surface layer and the free atmosphere, and 4) the moist-convective dynamics. Part III employs sensitivity experiments, as well as a further analysis of the results of the control simulation introduced here, to help define key physical processes, especially those responsible for the nighttime offshore convection.

Acknowledgments. This work was supported by NOAA Office of Global Programs (OGP) Pan American Climate Studies (PACS) Grant NA96GP0051. Andrea Hahmann and Tom Rickenbach shared valuable expertise on mesoscale dynamics over the Amazon. The simulations were improved by discussions with Hui Su and Changhai Lu, and the paper was improved by two careful anonymous reviews.

APPENDIX

Propagation Mechanisms of Model Amazon Squall Lines

In many of our earlier model runs, the grid-1 eastern boundary was at 50°W, over the Amazon. Since the ECMWF reanalysis boundary conditions are linearly interpolated between 0000 and 1200 UTC analyses (0700 and 1900 LT), the low-level atmospheric temperature at the boundary did not rise during the day, as it did over the strongly heated land in the model's interior. As a result, the eastern boundary acted rather like a land–sea contrast, with a vigorous ''boundary breeze'' initiating strong, well-defined north–south Amazon squall lines

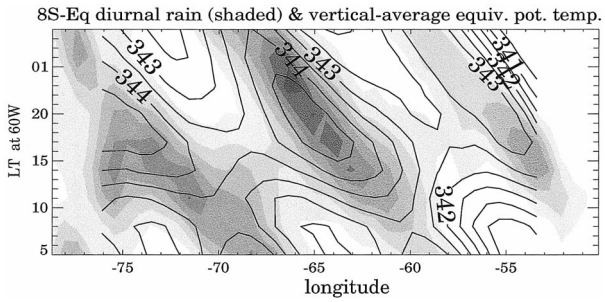

FIG. A1. Composite diurnal cycle of rainfall and vertical-average equivalent potential temperature θ_e vs longitude, averaged over 8°S–equator over the Amazon basin. Fields are from domain 1 of a simulation like the control but with the eastern boundary at 50°W. Amazon squall lines are apparent in rainfall rate (shading, linear grayscale) and surface–100-hPa-averaged θ_e (open contours, interval 0.5 K).

daily. While this daily strong two-dimensional excitation mechanism is unrealistic, Amazon squall lines do exist, both in nature (Garstang et al. 1994; Fig. 11b of Part I; Fig. 2 of MWX) and in the more realistic control run (Fig. 5b). For the limited, specific purpose of diagnosing propagation mechanisms, simulations with the 50°W boundary provide clearer, stronger signals than the control run. With a grid spacing of 72 km, the model produces rainfall almost exclusively by parameterized convection, not grid-resolved condensation. The model's squall-line propagation is not simply by cold-pool dynamics, in which rain-cooled outflow air propagates as a gravity current and triggers new convective cells at its leading edge. Rather, the propagation appears to involve the easterly jet near 650 hPa, as indicated by the theoretical model of Silva Dias and Ferriera (1992).

Two processes involving the 650-hPa easterly jet may be anticipated: horizontal advection of water substance, and critical-level ducting of low-level gravity waves (Lindzen and Tung 1976). To examine the advective effects of the jet, we consider the quantity $\langle\theta_e\rangle$, the mass-weighted vertical average over the model column (denoted by angle brackets $\langle\ \rangle$) of equivalent potential temperature θ_e, which is conserved in the atmosphere, even in the presence of condensation and evaporation. The only sources and sinks are radiation and surface flux,

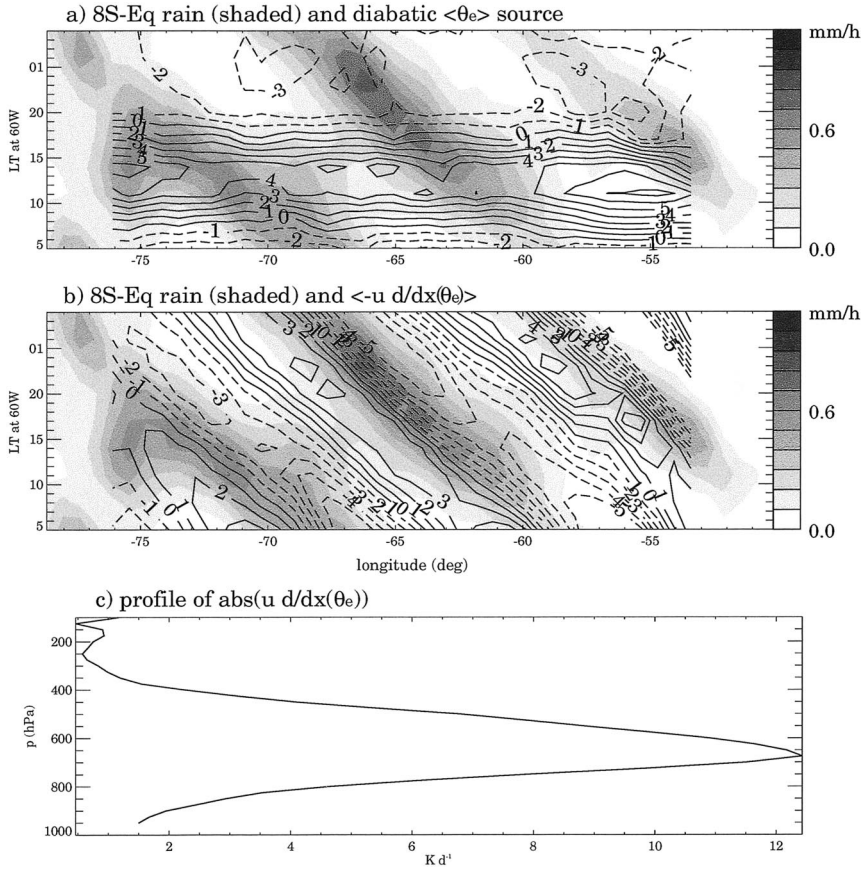

FIG. A2. Dominant terms in the vertically averaged budget of θ_e. Composite diurnal cycles of rain rate (shading) are repeated from Fig. A1 for reference in (a) and (b). (a) Source term (radiation and surface fluxes), computed from model fields as the total (local plus three-dimensional advection) tendency. (b) Horizontal advective tendency. (c) Profile of magnitude of horizontal advection of θ_e.

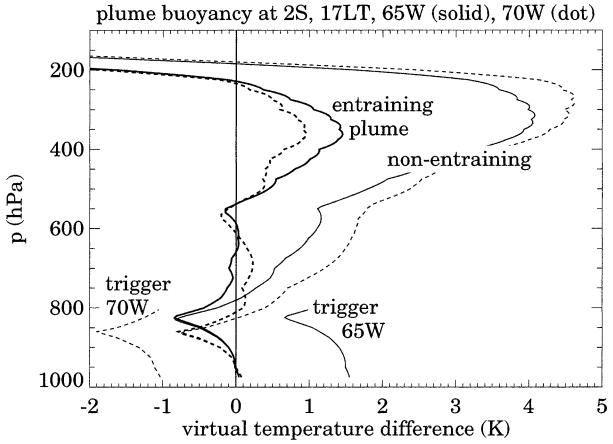

FIG. A3. Buoyancy of air lifted from the boundary layer, simulating the internal buoyancy computations in the KF convection scheme, in 10-day mean soundings at two longitudes along 2°S at 1700 LT. Solid lines are at 65°W, where maximum rainfall begins near 1700 LT; dotted lines are at 70°W, where rainfall occurs earlier in the day; light curves, undiluted parcel buoyancy; long heavy curves, with KF entrainment, plume radius 750 m; and short curves, plume buoyancy below 800 hPa plus the KF ''trigger function'' buoyancy offset (4.64 $w^{1/3}$, where w is vertical velocity at the lifting condensation level).

and the space and time variations of $\langle\theta_e\rangle$ are dominated by middle-tropospheric humidity variations. Figure A1 shows the 10-day composite diurnal evolution of rainfall (shaded) and $\langle\theta_e\rangle$ (labeled contours) for the 8°S–equator band. Both quantities exhibit standing and propagating parts, with longitudinal-mean maxima in the afternoon/evening hours, and westward propagation indicated by the contours sloping up and to the left. The two quantities are in phase, indicating that surface rainfall and middle-tropospheric humidity are closely associated.

Figure A2 repeats the rainfall contours (shaded) and shows dominant terms in a 10-day composite $\langle\theta_e\rangle$ budget at 2°S. Figure A2a shows the diabatic source of $\langle\theta_e\rangle$, the sum of surface flux and radiative heating (computed as the sum of the local tendency and three-dimensional advection). Positive tendencies are centered at about local noon at all longitudes, with negative tendencies at night. Clearly this is the source of the standing component of $\langle\theta_e\rangle$ changes. The vertically averaged horizontal advection $\langle -ud\theta_e/dx\rangle$ (Fig. A2b) leads rainfall and hence $\langle\theta_e\rangle$ by approximately a quarter cycle, and is the dominant cause of the propagating component of $\langle\theta_e\rangle$ variations (vertically averaged vertical advection is much smaller, not shown). The vertical profile of horizontal advective tendency is shown in Fig. A2c, and is clearly centered on the 675-hPa easterly jet. In summary, the easterly jet advects midlevel humidity anomalies and, hence, $\langle\theta_e\rangle$, which is observed to have a strong correlation with rainfall.

The physical linkage between midlevel humidity and convective rainfall is through entrainment in the Kain and Fritsch (1990, 1993; hereafter KF) convection scheme's buoyant plume model. Figure A3 depicts the buoyancy computed by a diagnostic version of the KF entraining plume with the same 750-m plume radius used in the model simulations, for model vertical soundings at two locations along 2°S at 1700 LT. The two longitudes are 70°W (dotted line), where maximum rainfall in the propagating bands occurs in the morning, and 65°W (solid line), where rainfall begins near 1700 LT, the time of the sounding. The lifting condensation level (low-level kink in the buoyancy profile) is lower at 70°W, where morning rains have left the boundary layer cooler and more humid, with θ_e slightly greater (2 K, not shown), leading to greater upper-level buoyancy of an *undiluted* lifted parcel (light lines). For the entraining plume, in contrast, upper-level buoyancy is greater at 65°W, owing to the effects of mixing with the more humid midlevel air there.

However, the KF scheme does not simply decide its rainfall rate based on entraining plume buoyancy: a complex trigger function is involved. Briefly, the grid-resolved vertical velocity at the lifting condensation level (about 850 hPa here) is converted, via a rather ad hoc formula, into a buoyancy increment for the plume. The approximate trigger function buoyancy increments at 65° and 70°W are indicated by the dashed and dotted lines below 800 hPa in Fig. A3. These are considerably larger than the differences between the entraining plume buoyancies, suggesting that a major reason for the greater rainfall at 65°W is not just midlevel humidity, but also low-level vertical velocity. This supposition was tested by disabling the trigger function on the KF scheme. In that case, the model did not display propagating Amazon squall lines.

Models in which convective heating and rainfall are assumed to be proportional to low-level vertical velocity (or convergence, or moisture convergence) are called convective instability of the second kind (CISK) models, and have been extensively studied both analytically and numerically. Silva Dias and Ferriera (1992, hereafter SDF) developed a linear CISK model in which Amazonian squall lines are represented as ''a packet of forced internal gravity waves.'' This description seems to apply well to the MM5 simulated rainbands, in which propagating vertical velocity features in the unsaturated, stably stratified lower troposphere modulate convective heating and rainfall through the trigger function. The existence and propagation of squall lines in the CISK model of SDF depended crucially on the strength and shape of the lower-tropospheric easterly winds. Neither that study nor this one devised a satisfying exact diagnosis of the role of the low-level easterly jet in the propagation of gravity waves, but the critical-level ducting theory of Lindzen and Tung (1976) certainly suggests itself. Westward moving gravity waves with phase speeds less than the easterly jet speed will be trapped or ducted at low levels, so if such waves induce parameterized convection whose heating in turn reinforces the waves, a propagating rainband may result. An example of the modulation of tropical convection by ducted low-

level gravity waves may be seen in recent work by Shige and Satomura (2001).

In summary, the propagation mechanisms appear to be mixed, at least in the model, with the moisture-advecting and wave-ducting roles of the easterly jet both contributing to these MM5-simulated Amazonian squall lines.

REFERENCES

Anthes, R. A., 1977: A cumulus parameterization scheme utilizing a one-dimensional cloud model. *Mon. Wea. Rev.,* **105,** 270–286.

Benjamin, S. G., and N. L. Seaman, 1985: A simple scheme for objective analysis in curved flow. *Mon. Wea. Rev.,* **113,** 1184–1198.

Chen, F., and J. Dudhia, 2001a: Coupling an advanced land surface–hydrology model with the Penn State–NCAR MM5 modeling system. Part I: Model implementation and sensitivity. *Mon. Wea. Rev.,* **129,** 569–585.

——, and ——, 2001b: Coupling an advanced land surface–hydrology model with the Penn State–NCAR MM5 modeling system. Part II: Model validation. *Mon. Wea. Rev.,* **129,** 587–604.

——, and Coauthors, 1996: Modeling of land-surface evaporation by four schemes and comparison with FIFE observations. *J. Geophys. Res.,* **101,** 7251–7268.

Cohen, J., M. Silva Dias, and C. Nobre, 1995: Environmental conditions associated with Amazon squall lines: A case study. *Mon. Wea. Rev.,* **123,** 3163–3174.

Dudhia, J., 1989: Numerical study of convection observed during the Winter Monsoon Experiment using a mesoscale two-dimensional model. *J. Atmos. Sci.,* **46,** 3077–3107.

——, 1993: A nonhydrostatic version of the Penn State/NCAR Mesoscale Model: Validation tests and the simulation of an Atlantic cyclone and cold front. *Mon. Wea. Rev.,* **121,** 1493–1513.

Garstang, M., H. L. Massie Jr., J. Halverson, S. Greco, and J. Scala, 1994: Amazon coastal squall lines. Part I: Structure and kinematics. *Mon. Wea. Rev.,* **122,** 608–622.

Greco, S., and Coauthors, 1990: Rainfall and surface kinematic conditions over central Amazonia during ABLE 2B. *J. Geophys. Res.,* **95,** 17 001–17 014.

Grell, G. A., 1993: Prognostic evaluation of assumptions used by cumulus parameterizations. *Mon. Wea. Rev.,* **121,** 764–787.

——, J. Dudhia, and D. R. Stauffer, 1994: A description of the fifth-generation Penn State/NCAR Mesoscale Model (MM5). NCAR Tech. Note NCAR/TN-398+STR, 138 pp.

Hong, S.-Y., and H.-L. Pan, 1996: Nonlocal boundary layer vertical diffusion in a medium-range forecast model. *Mon. Wea. Rev.,* **124,** 2322–2339.

Jacquemin, B., and J. Noilhan, 1990: Sensitivity study and validation of a land surface parameterization using the HAPEX-MOBILHY data set. *Bound.-Layer Meteor.,* **52,** 93–134.

Kain, J. S., and J. M. Fritsch, 1990: A one-dimensional entraining/detraining plume model and its application in convective parameterization. *J. Atmos. Sci.,* **47,** 2784–2802.

——, and ——, 1992: The role of convective ''trigger function'' in numerical forecasts of mesoscale convective systems. *Meteor. Atmos. Phys.,* **49,** 93–106.

——, and ——, 1993: Convective parameterization for mesoscale models: The Kain–Fritsch scheme. *The Representation of Cumulus Convection in Numerical Models, Meteor. Monogr.,* No. 46, Amer. Meteor. Soc., 165–170.

Lindzen, R. S., and K. K. Tung, 1976: Banded convective activity and ducted gravity waves. *Mon. Wea. Rev.,* **104,** 1602–1617.

Lopez, M. E., and W. E. Howell, 1967: Katabatic winds in the equatorial Andes. *J. Atmos. Sci.,* **24,** 29–35.

Loveland, T. R., J. W. Merchant, J. F. Brown, D. O. Ohlen, B. C. Reed, P. Olson, and J. Hutchinson, 1995: Seasonal land-cover regions of the United States. *Ann. Assoc. Amer. Geogr.,* **85,** 339–355.

Mahrt, L., and K. Ek, 1984: The influence of atmospheric stability on potential evaporation. *J. Climate Appl. Meteor.,* **23,** 222–234.

——, and H.-L. Pan, 1984: A two-layer model of soil hydrology. *Bound.-Layer Meteor.,* **29,** 1–20.

Mapes, B. E., T. T. Warner, and M. Xu, 2003a: Diurnal patterns of rainfall in northwestern South America. Part III: Diurnal gravity waves and nocturnal convection offshore. *Mon. Wea. Rev.,* **131,** 830–844.

——, ——, ——, and A. J. Negri, 2003b: Diurnal patterns of rainfall in northwestern South America. Part I: Observations and context. *Mon. Wea. Rev.,* **131,** 799–812.

Miller, D. A., and R. A. White, 1998: A conterminous United States multilayer soil characteristics dataset for regional climate and hydrology modeling. *Earth Interactions,* **2**. [Available online at http://EarthInteractions.org.]

Molinari, J., and M. Dudek, 1992: Parameterization of convective precipitation in mesoscale numerical models: A critical review. *Mon. Wea. Rev.,* **120,** 326–344.

Negri, A. J., L. Xu, and R. F. Adler, 2002: A TRMM-calibrated infrared rainfall algorithm applied over Brazil. *J. Geophys. Res.,* **107** (D20), 8048, doi:10.1029/2000JD000265.

Pan, H.-L., and L. Mahrt, 1987: Interaction between soil hydrology and boundary-layer development. *Bound.-Layer Meteor.,* **38,** 185–202.

Poveda, G., and O. J. Mesa, 2000: On the existence of Lloró (the rainiest location on Earth): Enhanced ocean–land–atmosphere interaction by a low-level jet. *Geophys. Res. Lett.,* **27,** 1675–1678.

Sadler, J. C., 1986: Analysis strategy for COADS and some comparison of products. *Proc. COADS Workshop,* Boulder, CO, NOAA Tech. Memo. ERL ESG-23, 116–120.

Satomura, T., 2000: Diurnal variation of precipitation over the Indo-China peninsula: Two-dimensional numerical simulation. *J. Meteor. Soc. Japan,* **78,** 461–475.

Schaake, J. C., V. I. Koren, Q. Y. Duan, K. Mitchell, and F. Chen, 1996: A simple water balance model (SWB) for estimating runoff at different spatial and temporal scales. *J. Geophys. Res.,* **101,** 7461–7475.

Shige, S., and T. Satomura, 2001: Westward generation of eastward-moving tropical convective bands in TOGA COARE. *J. Atmos. Sci.,* **58,** 3724–3740.

Silva Dias, M. A. F., and R. N. Ferreira, 1992: Application of a linear spectral model to the study of Amazonian squall lines during GTE/ABLE 2B. *J. Geophys. Res.,* **97,** 20 405–20 419.

Snow, J. W., 1976: The climate of northern South America. *Climates of Central and South America,* W. Schwerdtfeger, Ed., World Survey of Climatology, Vol. 12, Elsevier, 295–403.

Swanson, R., 1998: Regional-scale model climatology of the North American monsoon system. Ph.D. thesis, University of Utah, 159 pp.

Tripoli, G. J., and W. R. Cotton, 1989: Numerical study of an observed orogenic mesoscale convective system. Part I: Simulated genesis and comparison with observations. *Mon. Wea. Rev.,* **117,** 273–304.

Vizy, E. K., and K. H. Cook, 2002: Development and application of a mesoscale climate model for the tropics: the influence of sea surface temperature on the West African monsoon. *J. Geophys. Res.,* **107,** 4024, doi:10.1029/2001JD000510.

Wang, W., and N. L. Seaman, 1997: A comparison study of convective parameterization schemes in a mesoscale model. *Mon. Wea. Rev.,* **125,** 252–278.

Warner, T. T., and H.-M. Hsu, 2000: Nested-model simulation of moist convection: The impact of coarse-grid parameterized convection on fine-grid resolved convection. *Mon. Wea. Rev.*, **128,** 2211–2231.
——, Y.-H. Kuo, J. D. Doyle, J. Dudhia, D. R. Stauffer, and N. L. Seaman, 1992: Nonhydrostatic, mesobeta-scale real-data simulations with the Penn State University/National Center for Atmospheric Research mesoscale model. *Meteor. Atmos. Phys.*, **49,** 209–227.